Incorporating active transport of cellular cargo in stochastic mesoscopic models of living cells

ANDREAS HELLANDER[1], PER LÖTSTEDT *

[1] *Division of Scientific Computing, Department of Information Technology*
Uppsala University, SE-75105 Uppsala, Sweden
emails: andreas.hellander@it.uu.se, perl@it.uu.se

Abstract

We propose a new multiscale method to incorporate active transport of cargo particles in biological cells in stochastic, mesoscopic models of reaction-transport processes. Given a discretization of the computational domain, we find stochastic, convective mesoscopic molecular fluxes over the edges or facets of the subvolumes and relate the process to a corresponding first order finite volume discretization of the linear convection equation. We give an example of how this can be used to model active transport of cargo particles on a microtubule network by the motor proteins kinesin and dynein. In this way we extend mesoscopic reaction-diffusion models of biochemical reaction networks to more general models of molecular transport within the living cell.

1 Introduction

The implications of intrinsic noise for the function of biochemical reaction networks in the living cell has played a central role in computational systems biology in the last decade. Today it is widely recognized that discrete, mesoscopic models of biochemical kinetics offer a modeling advantage over the corresponding continuous macroscopic description commonly referred to as the reaction rate equations (RREs). The most frequently used model on the mesoscale is a continuous time, discrete space Markov process, realizations of which can be generated by kinetic Monte Carlo simulations with the stochastic simulation algorithm (SSA) due to Gillespie [17]. If the number of different chemical species as well as the (truncated) state space is small enough, direct solution of the chemical master equation (CME) is possible, see e.g. [8, 31].

The CME describes a well stirred system, and the basic assumption underlying that formulation is that many non-reactive molecular collisions occur between the reactive ones, such that each molecule has time to diffuse through the entire volume of the domain before reacting. When applicable, the well stirred assumption greatly simplifies modelling and simulation. However, many processes in a living cell can hardly be assumed to take place in a spatially homogeneous environment. In cell signalling, such as in mitogen activated protein kinase (MAPK) cascades, some reactions are localized to the membrane through scaffold proteins, while other reactions between freely diffusing proteins take place in the cytoplasm. Other components of the signalling cascade are localized to the nucleus. In such systems, spatial gradients of proteins may be formed, see [26] for a review. Examples of stochastic, mesoscopic models where spatial homogeneity cannot be assumed are found in [4, 7, 13, 35].

The CME can be generalized to include spatial effects and transport by diffusion by introducing a discretization of the computational domain into voxels, or subvolumes [23, Ch. XIV]. Each voxel in the mesh is assumed to be well stirred, and diffusion is treated as

*Financial support has been obtained from the Swedish Graduate School of Mathematics and Computing.

jumps from one voxel to an adjacent one. The equation governing the probability density function (PDF) in this case is called the reaction-diffusion master equation (RDME), and due to the enormous state space the only feasible approach to study the behavior of well-resolved models is by stochastic simulation. The next subvolume method (NSM) [7] is an efficient implementation of SSA for reaction-diffusion models with a fine spatial discretization. It has been implemented for structured, Cartesian meshes in the software mesoRD [19]. For general, unstructured tetrahedral meshes, jump coefficients were proposed in [9] and implemented in the software URDME [3]. Spatial stochastic simulations are generally very computationally demanding, and methods to speed up simulation have been proposed [2, 5, 15, 34]. How to best choose the sizes of the voxels for a given model is an open question. The smaller the subvolumes, the better the spatial resolution, but the RDME may break down in the limit of vanishing voxel sizes if the model contains second order reactions [21]. This issue is studied further in [11, 39]. Intuitively, the voxels have to be large enough to be able to incorporate bimolecular reactions: at least two molecules (and the reaction radius) must be able to fit inside the voxel, but yet small enough to be considered well stirred.

Even though the RDME offers an improvement over the well stirred model, diffusion is not the only way matter is transported in the eukaryotic cell: cargo can also be transported actively by energy dependent processes, utilizing the cytoskeleton structures and molecular motors. Various cargo such as vesicles, organelles, mRNA and proteins involved in signalling are transported by motor proteins that bind to the cargo and the cytoskeleton "track" and moves the cargo in a certain direction depending on the type of motor protein, for reviews see e.g. [20, 33, 40]. It is also believed that a cargo can bind to multiple, different motor proteins and in that way move bidirectionally on the microtubule fibers [42].

Theoretical models of MAPK cascades have recieved much attention in systems biology. Kholodenko suggests that only diffusion may be insufficient to propagate signals efficiently in MAPK cascades. He proposes that "[a] picture is emerging in which both endocytosis and scaffolding might be involved in the propagation of intracellular signals in a way such that vesicles and preassembled signalling complexes might move in a microtubule-dependent manner to appropriate cellular locations" [24]. In [25] he further argues that "simple diffusion may have a limited role in intracellular transport of signaling complexes".

Although active transport likely plays a prominent role in cellular organization and regulation in eukaryotic cells, mesoscopic models so far have not taken this into account. In this work, we extend the reaction-diffusion master equation framework to also include active transport. We propose a simple mesoscopic model for cargo transport on microtubule networks by motor proteins and we discuss how this model relates to a corresponding model and discretization scheme on the continuous, macroscopic scale. The same approach can be used for other transport processes of convective nature, and the computational framework we propose here is quite general: to simulate active transport in our framework amounts to deriving an appropriate macroscopic velocity field that models the microscopic process of interest via the mesoscale. It is not the purpose of this paper to draw any biological conclusions about the relative importance of diffusive and active transport in typical models in systems biology, but rather to introduce one way of incorporating both types of transport in simulations at the mesoscopic level. This will open up for further theoretical and computational studies of the above mentioned issue.

The remainder of this paper is organized as follows. Section 2 reviews the mathematical framework for modeling stochastic reaction-diffusion processes on the mesoscale and it introduces the RDME and its macroscopic counterpart, the reaction-diffusion equation. In Section 3, active transport is incorporated on the mesoscale. In the following section, we discuss how that model is related to a first order accurate and stable finite volume (FV) discretization of the macroscopic convection equation. In doing so we have derived a multiscale model for active molecular transport by simplifying a microscopic model for the mesoscale and then interpreted this model on the macroscale. Finally, one numerical example illustrates the methodology in Section 5.

2 The spatial master equation

In this section we will review the mathematical framework used to model biochemical reaction-transport processes on the mesoscale. We will also introduce the macroscopic counterpart. Both will be needed in later sections to develop a multiscale description of active transport processes inside the living cell.

Our computational domain Ω in space has a polygonal boundary $\partial\Omega$ and is covered by voxels (or subvolumes or computational cells or compartments) $\mathcal{V}_j,\ j = 1, \ldots, K$, and in every voxel there are N chemical species $X_{ij},\ i = 1, \ldots, N$. The length in 1D, the area in 2D, or the volume of a voxel in 3D is denoted by $|\mathcal{V}_j|$. The species react with each other and migrate to neighboring voxels e.g. by means of diffusion. The copy number of species i in voxel j at time t is $x_{ij}(t)$ and the time dependent state of the system is given by the array $\mathbf{x}(t)$ with $N \times K$ elements. The jth column of $\mathbf{x}$ is denoted by $\mathbf{x}_{\cdot j}$ and the ith row by $\mathbf{x}_{i\cdot}$. A change in the state of the system is caused by chemical reactions between the molecules in the same voxel and by molecules moving to adjacent voxels. Let $p(\mathbf{x}, t)$ be the probability density function (PDF) for the state $\mathbf{x}$ at t conditioned on some initial state. The time evolution of p satisfies a master equation. We follow the derivation of the master equation in [9].

2.1 Chemical reactions

A chemical reaction r introduces a change $\boldsymbol{\nu}_r$ in the state in voxel j from $\tilde{\mathbf{x}}_{\cdot j}$ to $\mathbf{x}_{\cdot j} = \tilde{\mathbf{x}}_{\cdot j} + \boldsymbol{\nu}_r$. A reaction occurs in a time interval $[0, dt]$ with probability $a_r(\tilde{\mathbf{x}}_{\cdot j})\, dt$ where a_r is the propensity for the reaction. In a system with only chemical reactions, p satisifes the chemical master equation (CME), see [16, Ch. 7], [23, Ch. V],

$$\begin{aligned}\frac{\partial p(\mathbf{x}, t)}{\partial t} &= \mathcal{M}p(\mathbf{x}, t) \equiv \\ &\sum_{j=1}^{K}\sum_{r=1}^{R} a_r(\mathbf{x}_{\cdot j} - \boldsymbol{\nu}_r)p(\mathbf{x}_{\cdot 1}, \ldots, \mathbf{x}_{\cdot j} - \boldsymbol{\nu}_r, \ldots, \mathbf{x}_{\cdot K}, t) \\ &- \sum_{j=1}^{K}\sum_{r=1}^{R} a_r(\mathbf{x}_{\cdot j})p(\mathbf{x}, t). \end{aligned} \tag{1}$$

The summation over the reactions is restricted to feasible reactions, i.e. those reactions emanating from or resulting in non-negative copy numbers. For the case of only one subvolume, $K = 1$, (1) describes the time evolution of the PDF in a well stirred system with volume $|\Omega|$.

2.2 Transport in space

To incorporate transport in the CME framework we take $K > 1$ and molecules are allowed to jump between adjacent voxels. In a system without chemical reactions, the state is changed only by molecules moving between the voxels. An example is diffusion where larger molecules are pushed by the smaller molecules in the solvent in Brownian motion. The migration of a molecule of species i from one voxel $\mathcal{V}_k$ to another voxel $\mathcal{V}_j$ can be written as a linear chemical reaction $X_{ik} \to X_{ij}$ with the propensity

$$b_{kj}(\mathbf{x}_{i\cdot}) = q_{kj}x_{ik}\ . \tag{2}$$

For this description to make sense, all coefficients q_{kj} should be non-negative, and they should be non-zero only if $\mathcal{V}_k$ and $\mathcal{V}_j$ are neighbours and have a face in common. In this way, jumps are only permitted between immediate neighbours in the mesh. Here, a face is defined as a point between two voxels in 1D, an edge in 2D or a facet in 3D. The coefficients may be different for different species and thus depend on i.

Let the state-change vector associated with the propensity b_{kj} be $\boldsymbol{\mu}_{kj}$. The master equation for the molecular motion can now be written in the same form as the CME in (1), see [16, Ch. 8], [23, Ch. XIV], [32],

$$\frac{\partial p(\mathbf{x},t)}{\partial t} = \mathcal{T}p(\mathbf{x},t) \equiv \sum_{i=1}^{N}\sum_{k=1}^{K}\sum_{j=1}^{K} b_{kj}(\mathbf{x}_{i\cdot} - \boldsymbol{\mu}_{kj})p(\mathbf{x}_{1\cdot},\ldots,\mathbf{x}_{i\cdot} - \boldsymbol{\mu}_{kj},\ldots,\mathbf{x}_{N\cdot},t) - b_{kj}(\mathbf{x}_{i\cdot})p(\mathbf{x},t). \tag{3}$$

Most components of $\boldsymbol{\mu}_{kj}$ are zero except for $\mu_{kj,k} = -1$ and $\mu_{kj,j} = 1$ if $\mathcal{V}_k$ and $\mathcal{V}_j$ are neighbors. For a voxel on the boundary $\partial\Omega$ of the computational domain there is no flux of molecules across the faces on $\partial\Omega$.

The full master equation for a system with both reactions and molecular transport is obtained from (1) and (3)

$$\frac{\partial p(\mathbf{x},t)}{\partial t} = \mathcal{M}p(\mathbf{x},t) + \mathcal{T}p(\mathbf{x},t) \tag{4}$$

and is widely known as the reaction-diffusion master equation (RDME) when $\mathcal{T}$ describes diffusive motion.

2.3 The macroscopic equations

The familiar reaction rate equations (RRE) for the concentrations ϕ_{ij} approximating the expected values $|\mathcal{V}_j|^{-1}x_{ij}$ of the species in $\mathcal{V}_j$ are obtained from the master equations (1) and (3) [16, 23]. For a model with only chemical reactions, we arrive at a system of nonlinear ordinary differential equations (ODEs) in $\mathcal{V}_j$

$$\frac{d\phi_{ij}}{dt} = \omega_i(\boldsymbol{\phi}_{\cdot j}) \equiv \sum_{r=1}^{R} \frac{\nu_{ri}}{|\mathcal{V}_j|} a_r(|\mathcal{V}_j|\boldsymbol{\phi}_{\cdot j}). \tag{5}$$

If a_r in (1) and (5) is replaced by b_{kj} in (2) and (3), then the macroscopic equations in a system with only molecular transport are

$$\begin{aligned}\frac{d\phi_{ij}}{dt} &= \sum_{k=1}^{K} \frac{\mu_{kj,j}}{|\mathcal{V}_j|} b_{kj}(|\mathcal{V}_k|\boldsymbol{\phi}_{i\cdot}) + \frac{\mu_{jk,j}}{|\mathcal{V}_j|} b_{jk}(|\mathcal{V}_j|\boldsymbol{\phi}_{i\cdot}) \\ &= \sum_{k=1}^{K} \frac{|\mathcal{V}_k|}{|\mathcal{V}_j|} q_{kj}\phi_{ik} - \left(\sum_{k=1}^{K} q_{jk}\right)\phi_{ij},\end{aligned} \tag{6}$$

since $q_{jj} = 0$. Let the matrix T have the elements $T_{jk} = q_{kj}|\mathcal{V}_k|/|\mathcal{V}_j| \geq 0,\ j \neq k$, and $T_{jj} = -\sum_{k\neq j} q_{jk} \leq 0$. Then (6) can be written

$$\frac{d\boldsymbol{\phi}_{i\cdot}^T}{dt} = T\boldsymbol{\phi}_{i\cdot}^T \tag{7}$$

for each species i, i.e. as a linear system of ODEs. Depending on the type of transport and on the type of mesh, q_{kj} are chosen differently. Next, we discuss the case when the transport process is diffusion.

2.4 Diffusion

In [9] the primal mesh is unstructured and consists of line segments in 1D, triangles in 2D , and tetrahedra in 3D. The voxels, or subvolumes, are cells in the dual mesh (see Figure 1).

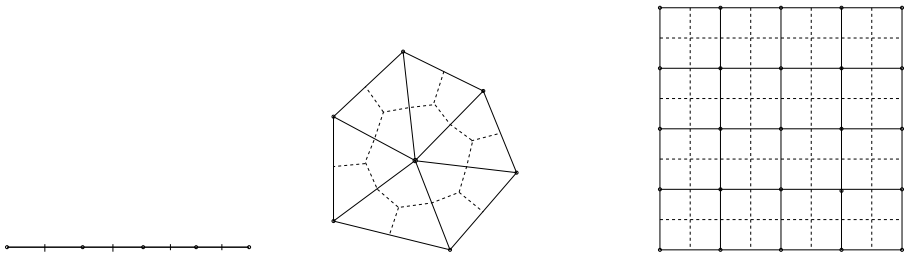

Fig. 1: The vertices (•), the edges in the primal mesh (solid lines) and the edges in the dual mesh or the voxel boundaries (dashed lines) in 1D (a), a triangular mesh in 2D (b), and Cartesian mesh in 2D (c).

In the interior of the mesh, the voxels have a vertex of the primal mesh in the center. If the molecular motion is diffusive then the macroscopic equation for the concentrations $\phi_i(\boldsymbol{\xi}, t), \boldsymbol{\xi} \in \Omega$, is the diffusion equation with the Laplacian Δ and diffusion coefficient γ

$$\frac{\partial \phi_i}{\partial t} = \gamma \Delta \phi_i = \gamma \nabla \cdot \nabla \phi_i, \ i = 1, \ldots, N. \tag{8}$$

With a finite element (FE) approximation of the solution of (8) using linear basis and test functions, the resulting equation in [9] is

$$\frac{\partial \boldsymbol{\phi}_{i\cdot}^T}{\partial t} = \gamma D \boldsymbol{\phi}_{i\cdot}^T, \ i = 1, \ldots, N, \tag{9}$$

where ϕ_{ij} is the concentration of species i at vertex j with coordinates $\boldsymbol{\xi}_j$. If the molecular transport is due to diffusion then $T = \gamma D$. Collect the coefficients q_{kj} in (2) in a matrix Q with $Q_{jk} = q_{kj}$ and let the positive elements of the diagonal matrix A be $A_{jj} = |\mathcal{V}_j|$. Then q_{kj} is defined by $Q = \gamma A D A^{-1}$, see [9].

The off-diagonal elements of D depend on the mesh and on the basis and test functions and should be non-negative as required for an interpretation of them as q_{kj} on the mesoscale, [9]. With a standard linear function space, there are algorithms in 2D for triangulations of quite complicated domains Ω almost satisfying this requirement, [12]. In 3D, generating tetrahedra with a FE discretization of the Laplacian with the guaranteed property $D_{jk} \geq 0, \ k \neq j$, with linear functions is a more difficult problem but some progress for simple boundaries is reported in [10].

In our present implementation in URDME [3], if there is a negative $D_{jk}, j \neq k$, then $-D_{jk}$ is added to the (j,k) component such that it vanishes and $-D_{jk}$ is subtracted from the diagonal D_{jj}. The correction is usually small. Since $D_{jk} = A_{jj}^{-1} S_{jk}$ and $D_{kj} = A_{kk}^{-1} S_{jk}$, the latter is also negative and is changed by $-A_{kk}^{-1} S_{jk}$. The symmetry of S is preserved after the modification of D. The new D-matrix is no longer a discretization of the Laplacian but nevertheless it approximates some kind of discretized diffusion with the properties: 1. the row sum is zero, $\sum_j D_{ij} = 0$, 2. the off-diagonal elements are non-negative, $D_{ij} \geq 0, \ i \neq j$, 3. a discrete maximum principle is satisfied, [28], 4. the non-negativity of the species is preserved, [28], 5. the discrete operator is local, and 6. it is conservative, $\sum_i A_{ii} D_{ij} = 0$.

3 Mesoscale transport of motor-cargo complexes on cytoskeletal filaments

Molecular motor proteins transport cargo on the "tracks" provided by the cytoskeletal filaments in eukaryotic cells. Due to their molecular nature, the fibers have a built-in direction in which motors travel, but different motors can travel in different directions on the same fiber type.

Originating from the microtubule organizing center (MTOC) near the cell nucleus, one type of fibers, microtubules, span the cytoplasm with their minus-end near the MTOC and the plus-end at the cell cortex. Cytoplasmic dynein motors walk on microtubules in the plus-to-minus direction. They transport cargo towards the cell interior, while kinesin motors transport cargo in the opposite direction towards the plasma membrane. For extensive overviews see e.g. [33, 37, 40] and the references and figures therein.

Another kind of fibers are found in the cortex of the cell immediately inside the outer cell membrane. Microfilaments made up of F-actin form an irregular meshwork of fibers on which the myosin family of motor proteins transport cargo. On average, the plus-ends of the actin filaments are directed towards the cell membrane and the minus-ends towards the cell interior.

In this section we propose how active transport of cargo-motor complexes on cytoskeletal fibers can be accounted for in the mesoscopic transport model in Section 2. We will not specify the type of cargo or the molecular motor protein bound to the cargo at this point. Initially, one new species, a cargo-motor complex, is introduced and we do not care about how this species was formed, what kind of cargo it describes and what type and how many motor proteins that are bound to it. The cargo-motor complex exists in two different forms: a cargo-motor complex that diffuses freely in voxel $\mathcal{V}_k$ is denoted by X_k^f, and a cargo-motor complex bound to a filament is denoted by X_k^b. The binding of X_k^f to a filament f in subvolume $\mathcal{V}_k$ is modeled as

$$X_k^f \xrightarrow{\omega^b(x_k^f, \bar{\rho}_k)} X_k^b, \tag{10}$$

where $\bar{\rho}_k$ is the mean fiber density in $\mathcal{V}_k$. The expression for the propensity ω^b is derived in (57) in Section 4.2.

An actin microfilament is approximately 6 nm wide and the larger microtubules are 24 nm wide. As a typical eukaryotic cell is of size $10 - 30$ μm, unless the mesh resolution is very fine in which case the RDME framework may be inappropriate [11, 21, 39], each voxel $\mathcal{V}_k$ in the mesh is likely to be populated by many fibers. The propensity for a cargo-motor complex to bind to a fiber in a voxel will be proportional to the total number of motor-filament binding sites, which is proportional to the total length of the fibers L_k in the voxel. Most motor proteins, such as conventional kinesin, myosin V or cytoplasmic dynein are processive: they will take several steps along the filament before detaching. For example, the *in vitro* processivity of kinesin is 0.8 – 1.2 μm [18]. In the mesoscopic model, this is reflected by the rate of an unbinding reaction

$$X_k^b \xrightarrow{k_d x_k^b} X_k^f, \tag{11}$$

where k_d is the rate constant and depends on the type of motor.

In Section 2, the mesoscopic model of diffusive transport was reviewed and the diffusion jump matrix D was introduced as derived in [9] which allowed for sampling of the process on a general, unstructured mesh. Here we want to arrive at a more general transport operator $\mathcal{T}$ as in (4) accounting for both diffusion and active transport,

$$\frac{\partial p(\mathbf{x}, t)}{\partial t} = (\mathcal{M} + \mathcal{T})p(\mathbf{x}, t), \quad \mathcal{T} = \mathcal{D} - \mathcal{C}. \tag{12}$$

where $\mathcal{C}$ describes active transport of the bound cargo-motor complex X^b on the fiber network. We propose how to construct an operator $\mathcal{C}$ that approximates the microscopic motion of the cargo-motor complex on the mesoscale. On the macroscale, there is a matrix C with the jump coefficients corresponding to D in (9).

As in the diffusive case, the transport process defined by $\mathcal{C}$ is modeled as a linear event in a Markov jump process

$$X_k^b \xrightarrow{b_{kj}^a(x_k^b)} X_j^b \tag{13}$$

that takes X_k^b to a neighboring voxel $\mathcal{V}_j$ and $b_{kj}^a(x_k^b) = q_{kj}x_k^b$, where q_{kj} is the jump rate constant and the value of the entry $-C_{jk}$ in the matrix C. Then we will be able to simulate both diffusion and active transport using existing methods and codes for generating realizations of the solution to the RDME, such as URDME [3], simply by supplying a more general Markov jump matrix $\gamma D - C$ as input to the code. The major complication here, compared to the purely diffusive case, is that the propensity function $b_{kj}^a(x_k^b)$ will ultimately depend on the geometry of the fiber network and on the particular model used for describing the interaction of the molecular motor proteins with the filaments.

As the stochastic model of the transport is a jump Markov process, the inverse of $b_{kj}^a(x_k^b)$ is interpreted as the expected time until one of the X_k^b molecules transitions to X_j^b,

$$b_{kj}^a(x_k^b) = (E[\tau_{kj}])^{-1}, \tag{14}$$

where τ_{kj} is the exit time

$$\tau_{kj} = \inf\{t \geq 0 : \text{one } X_k^b \text{ in voxel } \mathcal{V}_k \text{ leaves to voxel } \mathcal{V}_j\}, \tag{15}$$

or equivalently,

$$b_{kj}^a(x_k^b) = E[\text{the number of } X_k^b \text{ leaving to } \mathcal{V}_j \text{ per time unit}]. \tag{16}$$

If a detailed model and simulation method for the transport process on the microscale were available, this quantity could be estimated analytically or by simulation. That would amount to consider every voxel in the mesh and estimate the expectation in (14) in a Monte Carlo fashion. This is the idea in the heterogeneous multiscale method [6].

Next, a simple model of transport on microtubules by the motor protein kinesin is proposed. Our first and most fundamental simplifying assumption is to make the cytoskeleton *static*. No change in the topology of the network over time is permitted. With this assumption, the propensity function will be independent of time.

Each individual fiber in the computational domain Ω is labeled $f_m,\ m = 1, \ldots, M$. In each voxel in the mesh, a subset of the fibers will pass through. The subset associated with $\mathcal{V}_k$ is denoted by $\mathcal{F}_k$. The fibers are not straight, rigid cables. Internal stresses, even caused by the motor proteins themselves, make the fibers bend, and locally, the network can be disordered with fibers crossing each other.

A free cargo-motor complex diffuses in $\mathcal{V}_k$ until it either exits $\mathcal{V}_k$ or until it hits a fiber $f_m \in \mathcal{F}_k$ and binds to it. When it is bound to the fiber, it stays bound to it for a random *processivity time* τ_p. Then it moves on the filament at a random rate V with the expected value $E[V] = v$. The time τ_p is exponentially distributed with a parameter determined by the propensity of (11). If it has not exited the domain in time τ_p, it is released from the fiber and starts diffusing until it hits another fiber and rebinds or leaves the voxel (with propensity given by γD).

A bound cargo-motor complex X_k^b can be bound to any of the individual fibers f_m passing through that voxel. To keep track of which fibers are occupied with cargo, we introduce the auxiliary species X_{km}^b to be a cargo-motor complex bound to fiber $f_m \in \mathcal{F}_k$. We will also make the simplifying assumption that within the individual voxels, the fibers can be approximated by the straight line segments defined by the entry points of the fibers,

$\mathbf{y}_{km,en}$ and exit points $\mathbf{y}_{km,ex}$, see Figure 2. We can then parametrize f_m in $\mathcal{V}_k$ as $\mathbf{f}_{km}(\zeta) = \mathbf{y}_{km,en} + \zeta \mathbf{t}_{km}, \zeta \in [0, l_{km}]$, where $\mathbf{t}_{km}$ is the unit tangent vector $\mathbf{t}_{km} = l_{km}^{-1}(\mathbf{y}_{km,ex} - \mathbf{y}_{km,en})$ and l_{km} is the length of the fiber segment, $l_{km} = \|\mathbf{y}_{km,ex} - \mathbf{y}_{km,en}\|_2$. In other words, cargo particles bound to f_m in $\mathcal{V}_k$ move on $\mathbf{f}_{km}(\zeta)$ in the direction of $\mathbf{t}_{km}$ with the random speed V.

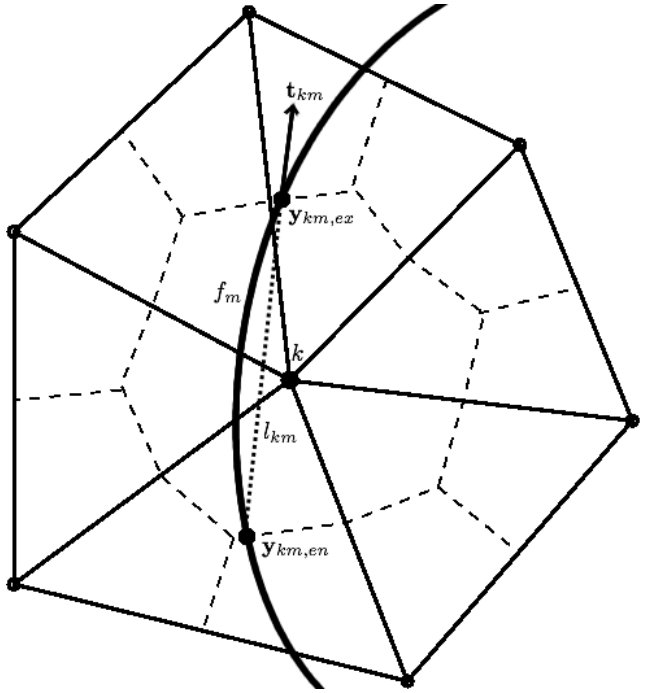

Fig. 2: Voxel in 2D showing a fiber, its entry and exit points, and the line segment and tangent vector used to parametrize the motor protein's movement on the fiber. Which point to define as the entry and exit point depends on the direction of travel of the motor protein.

Even for the same type of motor protein, e.g. kinesin, there is a variation in the observed speed with which individual motors travel [38]. In the mesoscopic model, we do not keep track of the intrinsic properties of individual molecules and fibers: that level of detail would be characteristic for a microscopic model. Rather, the variation in speed is modeled by the random variable V with some prescribed distribution and the speed is independent of the fiber and the position on the fiber. Then, looking at a separate voxel, given that a cargo particle is bound to a fiber segment f_m at the entry point $\mathbf{y}_{km,en}$ at time $t = 0$, the probability that the particle exits the voxel at $\mathbf{y}_{km,ex}$ before time s is

$$P(\tau_{km} \leq s) = P(V \geq l_{km}/s). \tag{17}$$

The expected time until a particle leaves on fiber f_m to $\mathcal{V}_j$ is

$$E_P[\tau_{km}] = l_{km}/v. \tag{18}$$

The model on the mesoscale is a Markov process and the exit time distribution of a molecule is assumed to be exponential

$$P_1(\tau_{km} \leq s) = 1 - \exp(-\frac{s}{E_P[\tau_{km}]}) = 1 - \exp(-\frac{sv}{l_{km}}). \tag{19}$$

The expression in (19) gives the probability that a single molecule in a voxel leaves before time s given that it was bound to the entry point $\mathbf{y}_{km,en}$ on f_m at time 0.

Using quantum-dot labelled kinesins, Seitz and Surrey [38] found the *in vitro* velocity distribution to be approximately normal with mean $0.56\mu m/s$. A standard deviation of $0.15\mu m/s$ gives a distribution close to that in [38, Fig. 1C]. Assuming that the speed follows a positive normal distribution, $V \sim \mathcal{N}_+(v, \sigma^2)$, the exit time from fiber f_m is by (17)

$$\begin{aligned} P_{1,\mathcal{N}}(\tau_{km} \le s) &= \frac{\beta}{\sigma\sqrt{2\pi}} \int_{l_{km}/s}^{\infty} \exp(-\frac{(\xi - v)^2}{2\sigma^2})\, d\xi \\ &= \frac{\beta}{2}\left(1 - \operatorname{erf}\left(\frac{v}{\sigma\sqrt{2}}\left(\frac{l_{km}}{sv} - 1\right)\right)\right), \text{ where} \\ \beta^{-1} &= \tfrac{1}{2}\left(1 - \operatorname{erf}(-\tfrac{v}{\sigma\sqrt{2}})\right). \end{aligned} \tag{20}$$

If l_{km}/sv is small then P_1 in (19) is close to 1 and if l_{km}/sv is large then $P_1 \approx sv/l_{km}$. Similary, if l_{km}/sv is small in (20), then $P_{1,\mathcal{N}}$ is close to 1 and if l_{km}/sv is large then according to [1, Ch. 7]

$$P_{1,\mathcal{N}} \approx \frac{\beta\sigma s}{2l_{km}\sqrt{2\pi}} \exp(-\frac{l_{km}^2}{2\sigma^2 s^2}).$$

Figure 3 shows a comparison between the exit distribution in (20) and that in (19) for different values of the parameter l_{km}/v. The error is the relative error $\|P_1 - P_{1,\mathcal{N}}\|_1/\|P_1\|_1$ in the ℓ_1-norm and we have used $\sigma = 0.15\mu m/s$. As can be seen, the exponential distribution approximates the distribution in (20) fairly well for a wide range of parameters, but performs best for small l_{km}/v. With a finer mesh, l_{km} is shorter and l_{km}/v smaller.

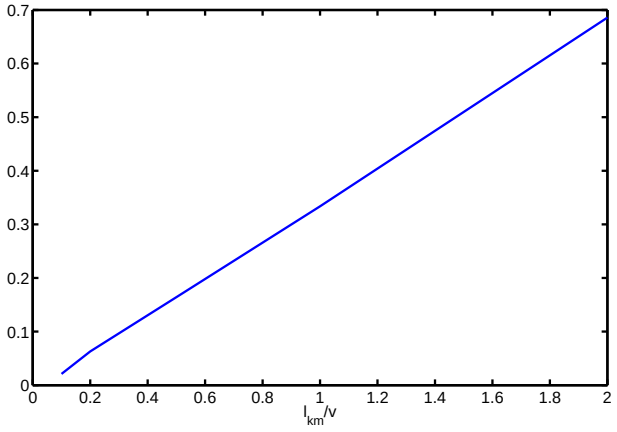

Fig. 3: The relative difference between the exponential distribution P_1 in (19) and the distribution $P_{1,\mathcal{N}}$ in (20) measured as $\|P_1 - P_{1,\mathcal{N}}\|_1/\|P_1\|_1$.

In a voxel with several cargo-motor complexes bound to f_m, let x_{km}^b be the copy number of X_{km}^b. Using the fact that the distribution of the minimum of independent exponential random variables is again exponential with parameter being the sum of the individual parameters, we obtain the conditional probability that the X_{km}^b complex that leaves the voxel first on f_m leaves before s

$$P(\tau_{km} \le s \mid X_{km}^b = x_{km}^b) = 1 - \exp(-\frac{svx_{km}^b}{l_{km}}). \tag{21}$$

Note that for $x_{km}^b = 0$, $P(\tau_{km} \le s \mid X_{km}^b = x_{km}^b) = 0$ for any finite s. This reflects the fact that if no molecules occupy the fiber, the mean exit time is $+\infty$, and the propensity in the Markov process takes the value zero.

We do not want to keep track of how many numbers of cargo-motor complexes that are bound to the individual fibers, since this introduces a lot of additional species X^b_{km} in the model and increases the computational time. Instead, we introduce the probabilities

$$p_{km} = P(X^b_k \text{ is bound to the entry point of fiber } f_m \text{ at } t = 0) \tag{22}$$

with $p_{km} > 0$. Then, assuming that cargo particles are independent of each other, and given that $X^b_k = \sum_{f_m \in \mathcal{F}_k} X^b_{km} = x^b_k$, the random vector $\bar{\mathbf{X}}^b_k = (X^b_{km})_{f_m \in \mathcal{F}_k}$ has a multinomial distribution with probabilities $\mathbf{p}_k = (p_{km})_{f_m \in \mathcal{F}_k}$ and total number ofm "trials" x^b_k. The marginal distribution of X^b_{km} is the binomial distribution with parameters p_{km} and x^b_k and τ_{km} in (21) is distributed according to

$$\tau_{km} \mid X^b_{km} = x^b_{km} \sim Exp(\frac{svx^b_{km}}{l_m}) \text{ with } X^b_{km} \sim Bin(x^b_k, p_{km}). \tag{23}$$

Again, to get the exit time distribution in the Markov model for $x^b_k \geq 1$, we approximate the distribution of τ_{km} in (23) with an exponential with mean

$$E[\tau_{km}] = E[E[\tau_{km}|X^b_{km}]] = E[l_{km}/(vX^b_{km})] = l_{km}/(vp_{km}x^b_k) \tag{24}$$

and we arrive at

$$P(\tau_{km} \leq s \mid X^b_k = x^b_k) = 1 - e^{-\frac{svx^b_k p_{km}}{l_{km}}}. \tag{25}$$

If $x^b_k = 0$, then $P(\tau_{km} \leq s \mid X^b_k = x^b_k) = 0$ as in (21).

If the number of molecules x^b_k is large, then X^b_{km} in (23) is approximately $\mathcal{N}(x^b_k p_{km}, x^b_k p_{km}(1-p_{km}))$ by the central limit theorem. The conditional distribution in (25) is close to that obtained directly from (23)

$$\begin{aligned} P(\tau_{km} \leq s \,|\, X^b_k = x^b_k) &= \sum_{j=0}^{x^b_k} \frac{x^b_k!}{j!(x^b_k - j)!} p^j_{km}(1-p_{km})^{x^b_k - j}(1 - e^{-\frac{svj}{l_{km}}}) \\ &\approx \int_{-\infty}^{\infty} \frac{1}{\sigma\sqrt{2\pi}} e^{-(\zeta - x^b_k p_{km})^2/2\sigma^2}(1 - e^{-\frac{sv\zeta}{l_{km}}})\, d\zeta \\ &\approx 1 - e^{-\frac{svx^b_k p_{km}}{l_{km}}}, \end{aligned}$$

with $\sigma = x^b_k p_{km}(1-p_{km})$.

Now, p_{km} is the fraction of the total number of bound molecules in $\mathcal{V}_k$ binding to fiber f_m. The distribution of the time τ_{kj} when the first cargo-motor complex leaves from $\mathcal{V}_k$ to $\mathcal{V}_j$ is the distribution for the minimum exit time among all fibers leaving $\mathcal{V}_k$ on the face in common with $\mathcal{V}_j$

$$P(\tau_{kj} \leq s | X^b_k = x^b_k) = 1 - \exp(-\sum_{f_m \in \mathcal{F}_{k\cap j}} \frac{svx^b_k p_{km}}{l_{km}}), \tag{26}$$

where $\mathcal{F}_{k\cap j} = \mathcal{F}_k \cap \mathcal{F}_j$ is the set of fibers exiting through the face between $\mathcal{V}_k$ and $\mathcal{V}_j$. This means that the propensity function in (14) is given by

$$b^a_{kj}(x^b_k) = q_{kj}x^b_k = \sum_{f_m \in \mathcal{F}_{k\cap j}} \frac{vx^b_k p_{km}}{l_{km}}. \tag{27}$$

We have assumed that there is equal probability for a molecule to enter a voxel on any of the fibers starting at a face and directed into the voxel. Then the probability to exit from the voxel must be equal on any of the fibers directed outward from the voxel. The number of molecules to leave on a fiber in a time interval $[0, \Delta t]$ is Poisson distributed with parameter $vx_k^b p_{km} \Delta t / l_{km}$. For the probability to be equal for all $f_m \in \mathcal{F}_{k\cap j}$ we require that $p_{km}/l_{km} = p_k$. Since $\sum_m p_{km} = p_k \sum_m l_{km} = p_k L_k = 1$, we infer

$$p_{km} = l_{km}/L_k. \tag{28}$$

Hence, the expression for the transport propensity is

$$b_{kj}^a(x_k^b) = q_{kj} x_k^b = \sum_{f_m \in \mathcal{F}_{k\cap j}} \frac{v x_k^b}{L_k} = \frac{N_{kj} v x_k^b}{L_k}. \tag{29}$$

Here, the total number of fibers exiting through the face shared by $\mathcal{V}_k$ and $\mathcal{V}_j$ is $N_{kj} = |\mathcal{F}_{k\cap j}|$.

Along with the binding reaction (10) and the unbinding reaction (11) this lets us simulate cargo movement by motor proteins on a network of microtubule filaments. The direction of motion depends on the type of motor protein. Note that given a filament network structure and a mesh, the matrix C can be assembled from (29) by counting the number of fibers N_{kj} exiting through each face in the mesh and measuring the total length of the filaments in each voxel. The face between voxels k and j may have fibers going in the opposite direction with $N_{jk} > 0$. They give rise to a non-zero b_{jk} and a corresponding non-zero entry C_{jk} in the C-matrix. The flow of particles across the interface can then be interpreted as a combination of convection and diffusion on the filaments.

Whether the fiber is exiting or entering the voxel depends on the nature of the motor protein that is modeled. Such a procedure could still pose practical difficulties but by using advanced image analysis techniques it is possible to track the filament fibers in a 3D reconstruction of the cytoskeleton. A method for detailed simulation of fibers at a microscopic level is developed in [36]. The resulting fiber networks can be used in our mesoscopic transport model.

The model proposed in this section relies on certain simplifications. For example, there is evidence that many types of cellular cargo move bidirectionally on microtubules [42]. This is accomplished by having multiple motors binding to the same cargo. However, it is not clear how the different motors are regulated to achieve a net transport to a certain location. One way to incorporate bidirectional transport is by introducing several distinct states for a cargo-motor complex when bound to the filament. A cargo-motor complex could be in a kinesin binding state and then converted to a dynein binding state with some probability. This would be a reasonable treatment if only one motor is interacting with the fiber at any time. Another possibility is to allow for a more general velocity distribution with diffusion on the fiber letting the cargo-motor complex move backward with some probability. This approach is more appropriate if motors bind simultaneously to the filament and engage in a "tug of war". Ultimately, how to model this phenomenon will depend on the underlying mechanistic model of regulation.

We have tacitly assumed that, whenever a cargo-motor complex encounters a crossing between two tracks, the complex continues on its present track. In reality, cargo can be transfered between filaments. A cargo destined for the cell membrane has to switch from kinesin on microtubules to myosin Va when reaching the actin filaments at the cell cortex. *In vitro* studies suggest that both at actin-microtubule intersections and at microtubule-microtubule intersections, cargo-motor complexes frequently switch tracks [37]. We are not currently incorporating this feature in this first, simple model, but could do so by assigning a probability for switching and explicitly accounting for crossings by modifying (18).

4 Relation to the macroscale

In this section we show how the mesoscopic molecular fluxes derived in the previous section relate to a discretization of a convection equation on the macroscale. Mesoscopic fluxes similar to those in (27) and (29) are obtained from a continuous velocity field suggesting a simpler way of obtaining mesoscopic jump propensity functions on general meshes.

4.1 Macroscopic transport and the finite volume method

If the chemical species are transported on the macroscale by a velocity field $\mathbf{v}(\boldsymbol{\xi})$ in Ω, then the equation for the time evolution of $\phi_i(\boldsymbol{\xi}, t)$ is

$$\frac{\partial \phi_i}{\partial t} + \nabla \cdot (\mathbf{v}\phi_i) = 0,\ i = 1, \ldots, N. \tag{30}$$

The velocity may be different for different species and can be zero for some i. As an example, take a spherical cell with a spherical void in the center representing the nucleus and introduce a spherical coordinate system (r, φ, θ). Assume that ϕ_i is independent of the angles φ and θ and that species i is propagated by the constant, positive velocity v_r along the r-axis. In that coordinate system, the equation (30) for $\phi_i(r, t)$ is

$$\frac{\partial \phi_i}{\partial t} + \frac{v_r}{r^2}\frac{\partial r^2 \phi_i}{\partial r} = 0. \tag{31}$$

Let the initial concentration in Ω be zero and let the concentration $\psi_i(t)$ be generated at the membrane of the nucleus at $r = r_0$. Then the solution of (31) is

$$\phi_i(r, t) = \frac{r_0^2}{r^2}\psi_i(t - (r - r_0)/v_r),\ r \geq r_0. \tag{32}$$

There is a wave propagating from the inner boundary of the cell cytoplasm at $r = r_0$ to the outer cell boundary at $r = r_1 > r_0$. What was generated at the nucleus appears there with an amplitude reduced by r_0^2/r_1^2 at a time delayed by $(r_1 - r_0)/v_r$.

In a finite volume (FV) method, (30) is integrated over one voxel $\mathcal{V}_j$ and then Gauss' theorem is invoked to obtain

$$\int_{\mathcal{V}_j} \frac{\partial \phi_i}{\partial t}\, d\Omega + \int_{\mathcal{V}_j} \nabla \cdot (\mathbf{v}\phi_i)\, d\Omega = \frac{\partial}{\partial t}\int_{\mathcal{V}_j} \phi_i\, d\Omega + \int_{\partial \mathcal{V}_j} \mathbf{n} \cdot \mathbf{v}\phi_i\, dS = 0. \tag{33}$$

The unit normal at the face $\partial \mathcal{V}_j$ pointing out from $\mathcal{V}_j$ is denoted by $\mathbf{n}$. The polygonal $\partial \mathcal{V}_j$ consists of a number of faces shared by voxel j and voxel k which belongs to the set $\mathcal{N}_j$ of immediate neighbors of j. Each section on the boundary $\partial \mathcal{V}_j \cap \partial \mathcal{V}_k$ may consist of a number of subsections $e_{jk}^{\ell},\ \ell = 1, \ldots, \Lambda_{jk}$, or edges in 2D and facets in 3D, see Fig. 4.1.a. An edge in 2D is straight and a facet in 3D is planar with constant normal $\mathbf{n}_{jk}^{\ell}$. In order to simplify the notation, we henceforth assume that $\Lambda_{jk} = 1$ and drop the superscript ℓ but all formulas and results can be generalized to the case with $\Lambda_{jk} > 1$. Let the average of ϕ_i in $\mathcal{V}_j$ be

$$\bar{\phi}_{ij} = |\mathcal{V}_j|^{-1} \int_{\mathcal{V}_j} \phi_i\, d\Omega. \tag{34}$$

If the integral over $\partial \mathcal{V}_j$ in (33) is approximated using $\bar{\phi}_{ij}$, we have derived a discretization of (30) with the FV method. The simplest choice is to evaluate $\mathbf{v}$ at the center of e_{jk} to obtain $\mathbf{v}_{jk}$ and let

$$\int_{\partial \mathcal{V}_j} \mathbf{v} \cdot \mathbf{n}\phi_i\, dS \approx \sum_{k \in \mathcal{N}_j} |e_{jk}| g(\mathbf{v}_{jk} \cdot \mathbf{n}_{jk}, \bar{\phi}_{ij}, \bar{\phi}_{ik}), \tag{35}$$

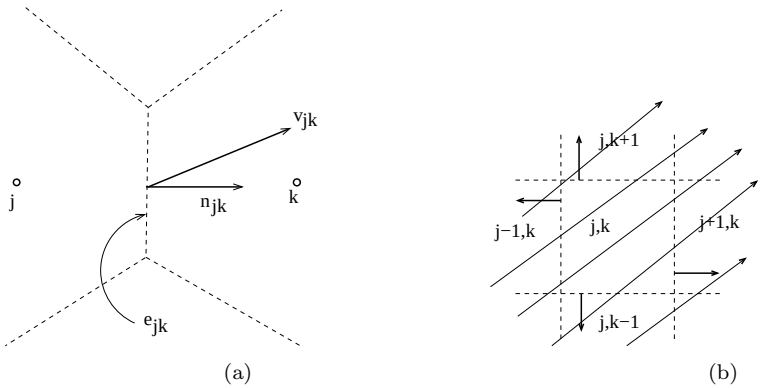

Fig. 4: (a) The face between voxels j and k. (b) A voxel in a Cartesian mesh with normals on the edges and the constant velocity field.

where $|e_{jk}|$ is the length or area of e_{jk} and the flux function is

$$g(x,y,z) = \frac{1}{2}x(y+z) + \frac{1}{2}|x|(y-z) = \begin{cases} xy & x \geq 0, \\ xz & x < 0. \end{cases} \tag{36}$$

The flux in (35) at a face is the normal velocity x times the average of the concentrations $\frac{1}{2}(y+z)$ plus a diffusive term $\frac{1}{2}|x|(y-z)$ to stabilize the scheme. The flux is [14, 30]:

1. consistent, $\zeta(\mathbf{v}\cdot\mathbf{n}, y, y) = \mathbf{v}\cdot\mathbf{n}y$,
2. conservative, $\zeta(\mathbf{v}\cdot\mathbf{n}, y, z) = -\zeta(-\mathbf{v}\cdot\mathbf{n}, z, y)$,
3. monotone, it is nonincreasing when z increases.

At an outflow boundary of $\partial\mathcal{V}_j$ with $\mathbf{v}_{jk}\cdot\mathbf{n}_{jk} \geq 0$ the flux is $\mathbf{v}_{jk}\cdot\mathbf{n}_{jk}\bar{\phi}_{ij}$ and at an inflow boundary with $\mathbf{v}_{jk}\cdot\mathbf{n}_{jk} < 0$ we take $\mathbf{v}_{jk}\cdot\mathbf{n}_{jk}\bar{\phi}_{ik}$. By combining (33), (34), and (35), the equations for the concentrations are

$$\frac{\partial\phi_{ij}}{\partial t} + |\mathcal{V}_j|^{-1}\sum_{k\in\mathcal{N}_j}|e_{jk}|g(\mathbf{v}_{jk}\cdot\mathbf{n}_{jk}, \phi_{ij}, \phi_{ik}) = 0,\ j = 1,\ldots,K, \tag{37}$$

where the bar denoting the average of $\boldsymbol{\phi}_{i\cdot}$ has been removed to simplify the notation. The flux is defined by the conditions at the faces of the voxels and is the same for two adjacent voxels but with opposite sign.

If the total flux $\mathbf{n}\cdot\mathbf{v}\phi_i$ across the outer boundary $\partial\Omega$ vanishes, $\int_{\partial\Omega}\mathbf{n}\cdot\mathbf{v}\phi_i\,dS = 0$, then by Gauss' formula we obtain

$$\frac{\partial}{\partial t}\int_\Omega \phi_i\,d\Omega + \int_{\partial\Omega}\mathbf{n}\cdot\mathbf{v}\phi_i\,dS = \frac{\partial}{\partial t}\int_\Omega\phi_i\,d\Omega = 0. \tag{38}$$

The total amount of species i in Ω is conserved. The discretization (37) shares this property. Consider the sum of the flux terms on the right hand side in (35) over all the voxels. A flux over an inner voxel face appears twice in the sum with opposite signs and the sum of the fluxes over the faces on the boundary $\partial\Omega$ is zero. The area weighted sum of the concentration of species i in the computational domain is then by (37)

$$\frac{\partial}{\partial t}\sum_j \phi_{ij}|\mathcal{V}_j| + \sum_j \sum_{k\in\mathcal{N}_j} |e_{jk}| g(\mathbf{v}_{jk}\cdot\mathbf{n}_{jk}, \phi_{ij}, \phi_{ik}) = \frac{\partial}{\partial t}\sum_j \phi_{ij}|\mathcal{V}_j| = 0. \tag{39}$$

The total amount of ϕ_i is preserved also by the FV space discretization in (35) and (37).

The equation for the concentration vector in all voxels $\boldsymbol{\phi}_{i\cdot}$ is derived from (37)

$$\frac{\partial \boldsymbol{\phi}_{i\cdot}^T}{\partial t} + C\boldsymbol{\phi}_{i\cdot}^T = 0. \tag{40}$$

The matrix C can be written as $C = A^{-1}U$ where the components of U are obtained from (37)

$$\begin{array}{ll} U_{jk} & = \begin{cases} |e_{jk}|\mathbf{v}_{jk}\cdot\mathbf{n}_{jk}, & k\in\mathcal{N}_j\cap\{k \mid \mathbf{v}_{jk}\cdot\mathbf{n}_{jk} < 0\}, \\ 0, & \text{otherwise}, \end{cases} \quad k\neq j, \\ U_{jj} & = \sum_{k\in\mathcal{Q}_j} |e_{jk}|\mathbf{v}_{jk}\cdot\mathbf{n}_{jk},\ \mathcal{Q}_j = \mathcal{N}_j\cap\{k \mid \mathbf{v}_{jk}\cdot\mathbf{n}_{jk} > 0\}. \end{array} \tag{41}$$

The diagonal elements of U are all non-negative and the off-diagonal elements are non-positive. Let $\mathbf{e}_1 = (1, 1, \ldots, 1)^T$ and $\mathbf{e}_A = A\mathbf{e}_1$. It follows from (40) and (39) that $\partial \mathbf{e}_A^T \boldsymbol{\phi}_{i\cdot}/\partial t = 0$ and therefore

$$0 = \mathbf{e}_A^T C = \mathbf{e}_1^T A A^{-1} U = \mathbf{e}_1^T U, \tag{42}$$

i.e. $\mathbf{e}_1$ is a left eigenvector of U with eigenvalue 0 and the column sums of U are zero. The steady state solution of (40) and the right eigenvector of U corresponding to this eigenvalue depend on $\mathbf{v}$ but in a special case an explicit solution is possible.

Suppose that $\mathbf{v}$ and $\boldsymbol{\phi}_i$ are both constant and that $\boldsymbol{\phi}_i = \eta\mathbf{e}_1$. The normal at $\partial\Omega$ pointing out from Ω is $\mathbf{n}_{\partial\Omega}$. The inflow boundary of $\partial\Omega$ is defined by the parts where $\mathbf{v}\cdot\mathbf{n}_{\partial\Omega} < 0$. The boundary condition of $\boldsymbol{\phi}_{ij}$ at the inflow boundary is η. For a voxel j in the interior of Ω or on the boundary $\partial\Omega$

$$\begin{aligned} 0 &= \int_{\mathcal{V}_j} \nabla\cdot(\mathbf{v}\eta)\, d\Omega = \int_{\partial\mathcal{V}_j} \eta\mathbf{v}\cdot\mathbf{n}\, dS = \sum_{k\in\mathcal{N}_j} \eta|e_{jk}|\mathbf{v}\cdot\mathbf{n}_{jk} \\ &= \eta(U_{jj} + \sum_{k\in\mathcal{N}_j} U_{jk}) = \eta\sum_{k=1}^{K} U_{jk} = \eta(U\mathbf{e}_1)_j = \eta A_{jj}(C\mathbf{e}_1)_j\ . \end{aligned}$$

Thus, $\mathbf{e}_1$ is a right eigenvector of U and C with eigenvalue 0 and the row sum of the two matrices vanishes.

Consider a species with concentration ϕ in the voxel j, k in the Cartesian mesh in Figure 4.1b and let $\mathbf{v} = (v_1, v_2)^T$ be constant. Then the space discretization according to (37) is with $\mathbf{n} = (1,0), (-1,0), (0,1)$ or $(0,-1)$, the step size $\Delta x = |e_{jk}|$, and $|\mathcal{V}_j| = \Delta x^2$

$$\begin{aligned} &\frac{\partial\phi_{j,k}}{\partial t} + v_1\frac{\phi_{j,k} - \phi_{j-1,k}}{\Delta x} + v_2\frac{\phi_{j,k} - \phi_{j,k-1}}{\Delta x} \\ &\qquad \approx \frac{\partial\phi}{\partial t} + \mathbf{v}\cdot\nabla\phi = \frac{\partial\phi}{\partial t} + \nabla\cdot(\mathbf{v}\phi). \end{aligned} \tag{43}$$

The space discretization in (43) on a Cartesian mesh is an upwind approximation of the space derivatives in (30). The accuracy is of first order in Δx.

If both convection and diffusion are present, then T in (7) is $-C+\gamma D$, where D is defined by a FE discretization as in Section 2.4. The total number of i-molecules $\mathbf{e}_A^T\boldsymbol{\phi}_{i\cdot}$ is conserved with this T since it is conserved by C and D separately, see (41), (42), and [9, (3.4)].

For a meaningful interpretation of the elements of T on the mesoscale, we need a stable approximation on the macroscale producing non-negative concentrations of the species. The next theorem shows that our space discretizations C and D indeed have those properties.

The primal mesh can be represented as a graph consisting of the vertices in the mesh and the edges between them. A graph is connected if there is a path via the edges between any pair of vertices in the graph [41, p. 20]. If Ω is connected, then there is a mesh with a connected graph. Let the time-derivative in (7) be approximated by a θ-method at the discrete time points $t^{n+1} = t^n + \Delta t,\ n = 0, 1, \ldots$ with the time step Δt and $\theta \in [0, 1]$. The recursion for $\boldsymbol{\phi}_{i\cdot}^{n+1}$ approximating $\boldsymbol{\phi}_{i\cdot}(t^{n+1})$ in (7) is with $T = -C + \gamma D$

$$(\boldsymbol{\phi}_{i\cdot}^{n+1})^T = (\boldsymbol{\phi}_{i\cdot}^{n})^T + \Delta t T((1-\theta)(\boldsymbol{\phi}_{i\cdot}^{n+1})^T + \theta(\boldsymbol{\phi}_{i\cdot}^{n})^T),\ n = 0, 1, \ldots \tag{44}$$

With the notation $\boldsymbol{\phi} \geq 0$ for an array, the relation holds for every element of $\boldsymbol{\phi}$: $\phi_{ij} \geq 0$. Then the time discretization has the following properties:

Theorem Assume that $\gamma > 0$, that Ω is connected and that the mesh has a connected graph. Let the norm $\|\boldsymbol{\phi}\|_{1A}$ be defined by

$$\|\boldsymbol{\phi}\|_{1A} = \sum_{j=1}^{K} A_{jj}|\phi_j|.$$

Determine C by the FV method and D by the FE method with $D = A^{-1}W$ where $W_{jk} \geq 0,\ j \neq k$, and $W_{jj} = -\sum_{k\neq j} W_{jk} < 0$. Then there is one steady state solution $\boldsymbol{\phi}_{i\cdot}^{\infty}$ satisfying $T(\boldsymbol{\phi}_{i\cdot}^{\infty})^T = 0$ and positivity $\boldsymbol{\phi}_{i\cdot}^{\infty} > 0$. Advance the solution in time by (44). If the time step Δt is sufficiently small then the time integration preserves positivity, i.e. if $\boldsymbol{\phi}_{i\cdot}^{n} > 0$ then $\boldsymbol{\phi}_{i\cdot}^{n+1} > 0$, and $\|\boldsymbol{\phi}_{i\cdot}^{n}\|_{1A} = \|\boldsymbol{\phi}_{i\cdot}^{0}\|_{1A},\ n = 1, 2, \ldots$

Proof

1. An irreducible matrix is defined in [41, p. 20]. If the mesh has a connected graph, then γD is irreducible. Since $C_{jj} \geq 0$ and $C_{jk} \leq 0,\ j \neq k$, $T = -C + \gamma D$ is also irreducible. Let $S = -U + \gamma W$ such that $T = A^{-1}S$. Then $S_{jj} < 0$ and $S_{jk} \geq 0, j \neq k$. Since $U^T\mathbf{e}_1 = W^T\mathbf{e}_1 = 0$, we have $S^T\mathbf{e}_1 = 0$ and $\sum_k (S^T)_{jk} = \sum_j S_{jk} = 0$. By Gershgorin's theorem, [41, p. 16], an eigenvalue $\lambda(S^T)$ belongs to the union of circles

   $$|\lambda(S^T) - S_{kk}| \leq \sum_{j\neq k} S_{jk} = -S_{kk},\ k = 1, \ldots, K.$$

   Choose $\alpha = \max_j(-S_{jj})$. Since S^T and S have the same eigenvalues and at least one eigenvalue of S is zero, $R = \alpha I + S$ has the spectral radius $\rho(R) = \alpha$. Moreover, $R \geq 0$ and the matrix is irreducible. It follows from the Perron-Frobenius theorem, [41, p. 30], that there is an eigenvector $\boldsymbol{\phi}_\alpha > 0$ with a simple eigenvalue $\rho(R) = \alpha$ of R. Then $S\boldsymbol{\phi}_\alpha = 0$ and therefore, $T\boldsymbol{\phi}_\alpha = A^{-1}S\boldsymbol{\phi}_\alpha = 0$.

2. Rewrite (44) in the form

   $$(I - \Delta t(1-\theta)T)(\boldsymbol{\phi}_{i\cdot}^{n+1})^T = (I + \Delta t\theta T)(\boldsymbol{\phi}_{i\cdot}^{n})^T. \tag{45}$$

   Let $G = I - \Delta t(1-\theta)T$ and $H = I + \Delta t\theta T$. We have that G is irreducible, $G_{jj} > 0$ and $G_{jk} \leq 0, j \neq k$. If Δt is so small that G is diagonally dominant, then $G^{-1} > 0$ [41, p. 85]. Furthermore, $H > 0$ if Δt is sufficiently small. Hence, by (45) $(\boldsymbol{\phi}_{i\cdot}^{n+1})^T = G^{-1}H(\boldsymbol{\phi}_{i\cdot}^{n})^T > 0$.

3. By (45), (41), and the properties of D in Section 2.4 we obtain

$$\begin{aligned}\|\boldsymbol{\phi}_{i\cdot}^{n+1}\|_{1A} &= \mathbf{e}_A^T(\boldsymbol{\phi}_{i\cdot}^{n+1})^T = \mathbf{e}_A^T(\boldsymbol{\phi}_{i\cdot}^{n})^T + \mathbf{e}_A^T T((1-\theta)(\boldsymbol{\phi}_{i\cdot}^{n+1})^T + \theta(\boldsymbol{\phi}_{i\cdot}^{n})^T) \\ &= \mathbf{e}_A^T(\boldsymbol{\phi}_{i\cdot}^{n})^T = \|\boldsymbol{\phi}_{i\cdot}^{n}\|_{1A}.\end{aligned}$$

Apply this formula recursively. ■

The third claim in the theorem shows that the time integration is stable in a weighted ℓ_1-norm.

With a FE discretization of the diffusion and the FV discretization of the convection, it is proved in 2D in [14] that the solution of (7) with a particular time discretization similar to (44) converges to the solution of

$$\frac{\partial \phi_i}{\partial t} + \nabla \cdot (\mathbf{v}\phi_i) = \gamma \Delta \phi_i,\ i = 1, \ldots, N, \tag{46}$$

when the mesh size $\Delta x \to 0$ and the time step $\Delta t \to 0$. Among the assumptions on the approximations are that the FV method is consistent, conservative, and monotone, and the triangles in the primal mesh have non-obtuse angles, cf. (36) and Section 2.4.

The combined macroscopic reaction-convection-diffusion equation (RCDE) for the molecular concentrations in the voxels in the dual mesh is derived from (5), (9), and (40)

$$\frac{\partial \boldsymbol{\phi}_{i\cdot}^T}{\partial t} = \omega_i(\boldsymbol{\phi}) - C\boldsymbol{\phi}_{i\cdot}^T + \gamma D\boldsymbol{\phi}_{i\cdot}^T = \omega_i(\boldsymbol{\phi}) + T\boldsymbol{\phi}_{i\cdot}^T,\ i = 1, \ldots, N. \tag{47}$$

It is a space discretization of

$$\frac{\partial \phi_i}{\partial t} + \nabla \cdot (\mathbf{v}\phi_i) = \omega_i(\boldsymbol{\phi}) + \gamma \Delta \phi_i,\ i = 1, \ldots, N, \tag{48}$$

The corresponding mesoscale equation for the PDF is (4) with $\mathcal{T} = -\mathcal{C} + \mathcal{D}$. The matrices T, C, and D in (47) have the same structure as Q defining the mesoscopic coefficients q_{kj} for the molecular transport in (6). The coefficients defining the propensities on the mesoscale are then given by the positive off-diagonal elements of

$$Q = ATA^{-1} = -ACA^{-1} + \gamma ADA^{-1}. \tag{49}$$

Suppose that the number of molecules increases in the mesoscale trajectories generated by the PDFs in (4) for a finite mesh. Then the molecular concentrations converge to a solution of (47) by the results of Kurtz [29]. See [9, 15] for computational verifications of this.

4.2 Relations between the micro-, meso- and macroscales

According to the assumptions in Section 3 the fibers are straight lines. Furthermore, assume that the fibers do not cross each other such that their directions form a continuous vector field $\mathbf{t}(\mathbf{x})$ with $\|\mathbf{t}\|_2 = 1$ in Ω. The directions of each fiber $\mathbf{t}_{km}$ in Section 3 and Figure 2 is here assumed to vary smoothly in $\mathbf{t}(\mathbf{x})$. Introduce a coordinate system $\zeta_1, \zeta_2, \zeta_3$ in 3D with the ζ_1-axis along $\mathbf{t}$. The fiber density is $\rho(\mathbf{x})$ on a small surface with $\mathbf{t}(\mathbf{x})$ as its normal.

Partition a voxel j into cylinders with their axes in the ζ_1-direction and let ρ be independent of ζ_1. The number of fibers in a cylinder α with the bottom and top surfaces $\Delta\Gamma_\alpha$ in the $\zeta_2 - \zeta_3$ plane is $\rho\Delta\Gamma_\alpha$ and the height is $\zeta_{1\alpha}$. Let the number of cylinders increase and let $\Delta\Gamma_\alpha \to d\zeta_2 d\zeta_3$. The total length L_j of the fibers in all cylinders in $\mathcal{V}_j$ is then

$$L_j = \sum_{f_m \in \mathcal{F}_j} l_{jm} = \sum_\alpha \zeta_{1\alpha}\rho\Delta\Gamma_\alpha \to \int_{\mathcal{V}_j} \rho\, d\zeta_1 d\zeta_2 d\zeta_3 = \bar{\rho}_j |\mathcal{V}_j|, \tag{50}$$

where $\bar{\rho}_j$ is the mean value in voxel j.

The number of fibers crossing the face e_{jk} from $\mathcal{V}_j$ to $\mathcal{V}_k$ is N_{jk}. The fiber density on $\partial\mathcal{V}_{jk}$ is $\rho\mathbf{t}\cdot\mathbf{n}_{jk}$. The mean value of $\rho\mathbf{t}$ on e_{jk} is $\rho_{jk}\mathbf{t}_{jk}$, where $\mathbf{t}_{jk}$ is a unit vector. Hence,

$$N_{jk} = \int_{e_{jk}} \rho\mathbf{t}\cdot\mathbf{n}_{jk}\, dS = |e_{jk}|\bar{\rho}_{jk}\mathbf{t}_{jk}\cdot\mathbf{n}_{jk}. \tag{51}$$

If the sign of $\mathbf{t}\cdot\mathbf{n}_{jk}$ changes on e_{jk} then the mesh should be refined here. The mean $\bar{\rho}_{jk}$ is approximated by $\bar{\rho}_j$ and $\mathbf{t}_{jk}$ by $\mathbf{t}$ at the midpoint of e_{jk}. By (50) and (51), the mesoscopic coefficient in the convection propensity in (29) is

$$q_{jk} = \frac{N_{jk}v}{L_j} = \frac{v|e_{jk}|\mathbf{t}\cdot\mathbf{n}_{jk}}{|\mathcal{V}_j|} > 0. \tag{52}$$

For fibers entering voxel j from voxel k we have

$$q_{kj} = \frac{v|e_{kj}|\mathbf{t}\cdot\mathbf{n}_{kj}}{|\mathcal{V}_k|} = -\frac{v|e_{jk}|\mathbf{t}\cdot\mathbf{n}_{jk}}{|\mathcal{V}_k|} > 0. \tag{53}$$

The mesoscopic propensity to transport molecules from one voxel to the adjacent one is independent of the fiber density but proportional to the number of bound molecules. This number depends on the number of fibers in the voxel.

The macroscopic interpretation of the mesoscopic coefficients in the convection matrix C is by (49), (52), and (53)

$$C_{jk} = -\frac{|\mathcal{V}_k|}{|\mathcal{V}_j|}Q_{jk} = -\frac{|\mathcal{V}_k|}{|\mathcal{V}_j|}q_{kj} = \frac{v|e_{jk}|\mathbf{t}\cdot\mathbf{n}_{jk}}{|\mathcal{V}_j|} < 0, \tag{54}$$

if the voxels j and k are neighbors and fibers are entering voxel j from k. Otherwise, $C_{jk} = 0$. The diagonal elements of C are

$$C_{jj} = -Q_{jj} = \sum_k q_{jk} = \sum_k \frac{v|e_{jk}|\mathbf{t}\cdot\mathbf{n}_{jk}}{|\mathcal{V}_j|} > 0. \tag{55}$$

Comparing (54) and (55) with (41) having the relation $C = A^{-1}U$ in mind, the conclusion is that the macroscopic velocity $\mathbf{v}$ is

$$\mathbf{v}(\mathbf{x}) = v\mathbf{t}(\mathbf{x}),\ \|\mathbf{v}\|_2 = v. \tag{56}$$

The binding and unbinding events (10) and (11) in a voxel are modeled as chemical reactions. The propensity for a molecule X_j^f to bind to the fibers in (10) is in d dimensions

$$\omega^b(x_j^a) = \tilde{k}_a\frac{L_j}{|\mathcal{V}_j|}x_j^a = \tilde{k}_a\bar{\rho}_j x_j^a = k_a\bar{\rho}_j x_j^a|\mathcal{V}_j|^{-1/d}N_A^{-1}, \tag{57}$$

if $\tilde{k}_a$ is an association rate per fiber length, N_A is Avogadro's number and k_a is expressed in $M^{-1}s^{-1}$. The dissociation of the cargo complex from the fiber depends only on the rate k_d and the copy number in (11).

In summary, we have obtained a relation between the microscopic properties of transport on microtubules, the jump coefficients in the mesoscopic propensities in the master equation (3), and the macroscopic velocity field $\mathbf{v}$ and a stable discretization of (30) on an unstructured mesh by a FV method. This suggests a way of modeling transport on the mesoscale by specifying a velocity field as in (56) that approximates the detailed properties of the fiber network. For any given mesh, the correct mesoscopic jump rate constants can then be obtained simply by discretizing the macroscopic convection equation with the FV method described above. In the next section we will give a computational example in which we use this procedure. A more accurate but also more complicated way of determining the mesoscopic rate constants is directly via (29) where the number of fibers crossing a face must be counted and their total length estimated.

5 Numerical example

In this section we consider two simple examples where active transport is modeled by a velocity field specified on the macroscale. In line with the discussion in the previous section, we use a FV discretization of the linear transport equation to derive the mesoscopic fluxes due to active transport. Diffusion events and reactions are treated in the model in the same way as described in Section 2 or in more detail in [9]. The simulations are carried out using NSM [7] as implemented in URDME [3].

5.1 Transport of cargo particles inside a cell

In a typical animal cell, the microtubules originate from the MTOC near the nucleus, and grow radially outwards with the minus end near the MTOC. Depending on the cell type, its average size is usually in the range $10-30\mu m$. In this numerical example, the computational domain discretized by tetrahedra is depicted in Figure 5. It consists of two concentric spheres with its centers at the origin of the coordinate system, the smaller one modeling the cell nucleus with radius $r_0 = 2\ \mu m$ and the larger one, with a radius of $r_1 = 7.5\ \mu m$, modeling the main cell body. The velocity field that the microtubule network gives rise to is modeled as a radially directed field. The network is densest near the nucleus, and it becomes progressively thinner as we approach the cell periphery. We assume that the filament network consists of a total number of M microtubule filaments originating uniformly from the nuclear membrane, and that the same number of filaments reach the plasma membrane. Let $\boldsymbol{\xi} = (\xi_1, \xi_2, \xi_3)$ be a point in a Cartesian coordinate system and let the filament density in the cytosol decay away from the nuclear membrane

$$\rho(\boldsymbol{\xi}) = \rho_0 + (\|\boldsymbol{\xi}\|_2 - r_0)\frac{\rho_1 - \rho_0}{r_1 - r_0}, \quad \rho_0 = M/S_A^n,\ \rho_1 = M/S_A^p,$$

where S_A^n and S_A^p are the surface areas of the nucleus and the cell, respectively. If the model of the fiber network had been based on an image of the cytoskeleton, the density and velocity field could have been estimated from that image. For the rate of transport on the fibers, we take $v = 0.5 \times 10^{-6}\ \mu m/s$, close to the average value for kinesin in [38]. The macroscopic velocity field is then given by

$$\mathbf{v}(\boldsymbol{\xi}) = \pm\frac{v}{\|\boldsymbol{\xi}\|_2}(\xi_1, \xi_2, \xi_3)^T.$$

The velocity field and the filament density for $M = 1000$ is depicted to the right in Figure 5.

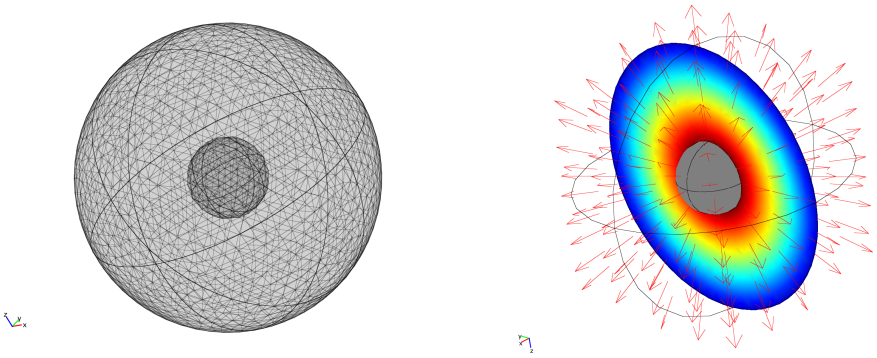

(a) (b)

Fig. 5: Computational domain (a) and velocity field for the cargo bound to a kinesin motor (b).

Since the focus here is on illustrating the modeling of active transport, we consider a simplified model consisting of a signal species S emanating at the plasma membrane. That signal can then be transported to the nuclear region, either by diffusion or active transport by dynein. To model the different kinds of transport, S will exist in two forms, freely diffusing S_f, and bound to filament S_b. Once inside the nucleus, the signal will initiate a series of events, eventually leading to the creation of a response species R. To avoid an unnecessarily complex model, we model the entry into the nucleus as a diffusion event over the nuclear membrane. The intermediate events leading to the creation of R are not modelled explicitly. When R exits the nucleus, it can diffuse through the cytoplasm, or be transported towards the plasma membrane on the filament network by a kinesin motor. In the same way as for the signal species, R is present in a freely diffusing state R_f or a microtubule-bound state R_b. Table 5.1 summarizes the reactions in the model. The parameters for the motor-microtubule interaction in the model are the binding rate of motor to fiber, $k_a = 2 \times 10^7\ M^{-1}s^{-1}$ [22], and the mean processivity time k_d. With a mean run length of $0.5 - 2\ \mu m$ and a mean velocity of $0.5 - 1\ \mu m/s$, a reasonable value of k_d for kinesin is $k_d = 1\ s^{-1}$. This is also the value in a simple model of kinesin's biochemical cycle in [38, Fig. 5]. For cytoplasmic dynein, it has been observed that the microtubule binding protein dynactin can increase the motor's processivity in vitro [27]. We use the same kinetic parameters for the velocity and processivity time of dynein as those for kinesin, and this is in accordance with the values obtained in [27] in the presence of dynactin.

Cytosol	$S_f \underset{k_d}{\overset{k_a}{\rightleftharpoons}} S_b \qquad R_f \underset{k_d}{\overset{k_a}{\rightleftharpoons}} R_b$
Nucleus	$S_f \xrightarrow{k_2} R_f$

Table 1: Reactions in the simple signal-response system described above. The rate constant k_a will take the value $2 \times 10^7\ M^{-1}s^{-1}$ in the experiments below, while $k_d = 1.0\ s^{-1}$ and $k_2 = 1.0\ s^{-1}$. The functional form of the propensity function for the forward cytosolic reactions is that given in (57) with $d = 3$.

With this construction, there is a one to one correspondence between the signalling species S and response species R. Whenever a R_f molecule reaches the plasma membrane, we let it fuse with the membrane and diffuse only on the membrane surface. For a R molecule to reach the membrane, a S molecule must be transported to the nucleus, be transformed into R, which then is transported back to the cell periphery. In order to illustrate the behavior of the system we define the response time to be the time until half of the initial number of $10^4 S$ molecules have been converted to R at the plasma membrane. By varying the total number of fibers M, we modulate the ratio of diffusive and active transport. To the left in Figure 6, we show for on trajectory the total number of R_f molecules at the plasma membrane as a function of time when varying the fiber density for a fixed diffusion constant, and to the right we show a comparison of the diffusion only case for a number of different diffusion constants to the case with both active and diffusive transport. As can be seen, the diffusion constant has to be increased one order of magnitude in order to achieve about the same response time as the case with $M = 2000$. Moreover, the higher diffusion constant, $\gamma = 10\mu m^2/s$ is not physiologically relevant for larger proteins or protein complexes in a crowded environment such as the cytosol.

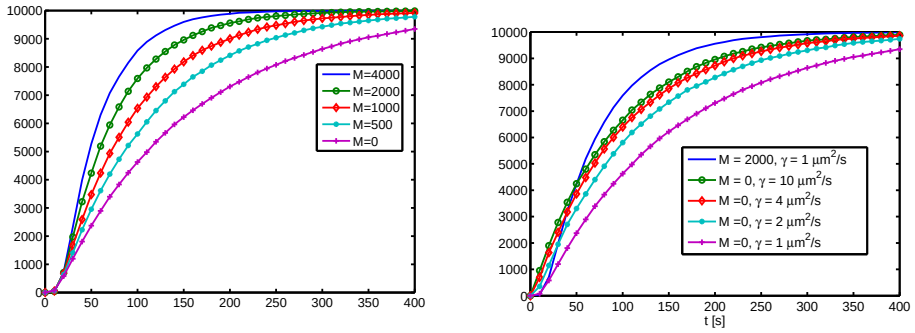

(a) (b)

Fig. 6: Response curves showing how the response species R accumulates at the cell membrane with varying filament density (a) and for different diffusion constants (b).

A key feature of the mesoscopic model is that it is stochastic. The response curves in Figure 6 all represent a single realization of the stochastic process, and they will vary slightly for different realizations of the process. To illustrate the kind of questions we can study using the stochastic model, we show the distribution of the response time for the system τ_R, estimated from 1000 realizations in Figure 7. To the left the case when $M = 2000$ and $\gamma = 1\ \mu m^2/s$ is displayed, and to the right when there is no active transport. From the CDFs in Figure 7, we obtain information of how likely the system is to show a certain response before some given time, which is of interest when addressing issues regarding e.g. robustness of a signalling network to noise.

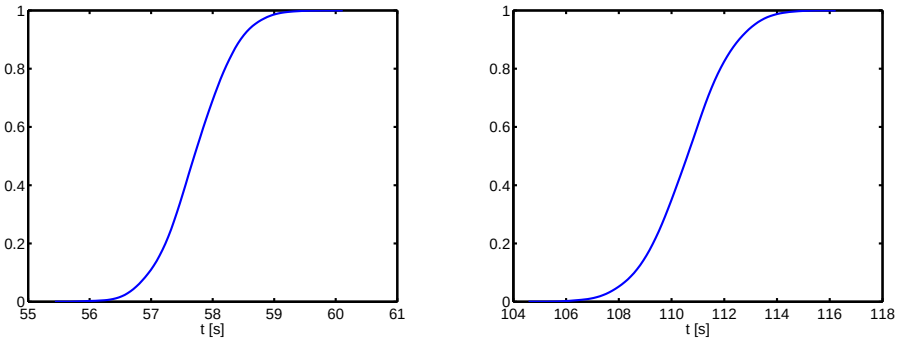

(a) (b)

Fig. 7: The cumulative distribution function for the response time of the system τ_R, for $M = 2000$ and $\gamma = 1\ \mu m^2/s$ (a) and for $M = 0$ and $\gamma = 1\ \mu m^2/s$.

This example is fictitious but it retains some key features of signalling cascade models such as those of MAPK cascades. We cannot draw any conclusions about the functioning of signalling networks merely from these simulations. However, we clearly see differences in the system response depending on the ratio of active and diffusive transport for the values of the constants we consider here.

6 Conclusions

In this paper we have developed a model that extends stochastic reaction-diffusion simulations on the mesoscale to include transport of cargo-motor complexes on filament networks.

We illustrated how such a mesoscopic description is obtained from the microscale, and further, by relating that mesoscale model to macroscale transport and convection, we arrived at a model of the filament network as a continuous velocity field. That gave us a convenient computational method in which one can obtain the jump rate constants in the mesoscopic model simply by assembling the first order upwind FV scheme for the macroscopic convection equation. This approach is very general, works equally well for structured and unstructured meshes, and integrates in a natural way with existing methodology to simulate reaction-diffusion processes on the mesoscale.

Throughout this paper we have assumed that the fiber network, and thus the velocity field, is stationary. During the course of a simulation, we could let the velocity field change at certain time points by updating the field and reassemble the matrix with jump rates. If the velocity field changes slowly on the time scale of the reaction dynamics, so that many stochastic events can be generated in between each velocity field update, this approach is feasible computationally.

In modeling the mesoscopic propensity due to transport on filaments, we made a few assumptions and simplifications. However, the computational framework we develop is more general than that particular model. A more detailed model can be implemented if one derives the mesoscopic propensity coefficients from the microscale description of transport and possibly also a macroscopic velocity field in the same spirit as we do here by incorporating more of the microscale features.

Even though the numerical example in this paper is modeling transport on filaments inside a cell, the same approach can obviously be used in other scenarios. The only requirement is that the modeler provides a velocity field that describes the transport process. For example, to simulate stochastic reaction-diffusion processes in a flowing fluid, the velocity field can be obtained easily by solving equations for the fluid motion. This approach would be particularly simple using the URDME software, since it is integrated with the powerful multiphysics simulation software COMSOL Multiphysics 3.5a (http://www.comsol.com).

References

[1] M. Abramovitz and I.A. Stegun. *Handbook of Mathematical Functions*. Dover, New York, 1970.

[2] Basil Bayati, Philippe Chatelain, and Petros Koumoutsakos. D-leaping: Accelerating stochastic simulation algorithms for reactions with delays. *Journal of Computational Physics*, 228(16):5908 – 5916, 2009.

[3] J. Cullhed, S. Engblom, and A. Hellander. The URDME manual version 1.0. Technical Report 2008-022, Dept of Information Technology, Uppsala University, Uppsala, Sweden, 2008. Available at `http://www.it.uu.se/research`.

[4] K. Doubrovinski and M. Howard. Stochastic model for Soj relocation dynamics in *Bacillus subtilis*. *Proc. Natl. Acad. Sci. USA*, 102:9808–9813, 2005.

[5] Brian Drawert, Michael J. Lawson, Linda Petzold, and Mustafa Khammash. The diffusive finite state projection algorithm for efficient simulation of the stochastic reaction-diffusion master equation. *J. Chem. Phys.*, 2010 (to appear).

[6] Weinan E and Björn Engquist. The heterogeneous multiscale method. *Commun. Math. Sci.*, 1(1):87–132, 2003.

[7] J. Elf and M. Ehrenberg. Spontaneous separation of bi-stable biochemical systems into spatial domains of opposite phases. *Syst. Biol.*, 1:230–236, 2004.

[8] Stefan Engblom. *Numerical Solution Methods in Stochastic Chemical Kinetics*. PhD thesis, Uppsala University, 2008.

[9] Stefan Engblom, Lars Ferm, Andreas Hellander, and Per Lötstedt. Simulation of stochastic reaction–diffusion processes on unstructured meshes. *SIAM J. Sci. Comput.*, 31(3):1774–1797, 2009.

[10] D. Eppstein, J. M. Sullivan, and A. Üngör. Tiling space and slabs with acute tetrahedra. *Comput. Geom.*, 27:237–255, 2004.

[11] Radek Erban and S. Jonathan Chapman. Stochastic modeling of reaction-diffusion processes: algorithms for bimolecular reactions. *Arxiv preprint arXiv:0903.1298*, 2009.

[12] H. Erten and A. Üngör. Quality triangulations with locally optimal steiner points. *SIAM J. Sci. Comput.*, 31:2103–2130, 2009.

[13] D. Fange and J. Elf. Noise-induced min phenotypes in *E. coli*. *PLoS Comput. Biol.*, 2:637–648, 2006.

[14] M. Feistauer, J. Felcman, M. Lukáčová-Medvid'ová, and G. Warnecke. Error estimates for a combined finite volume-finite element method for nonlinear convection-diffusion problems. *SIAM J. Numer. Anal.*, 36:1528–1548, 1999.

[15] Lars Ferm, Andreas Hellander, and Per Lötstedt. An adaptive algorithm for simulation of stochastic reaction-diffusion processes. *J. Comput. Phys.*, 229(2):343–360, 2010.

[16] C. W. Gardiner. *Handbook of Stochastic Methods*. Springer Series in Synergetics. Springer-Verlag, Berlin, 3rd edition, 2004.

[17] D. T. Gillespie. A general method for numerically simulating the stochastic time evolution of coupled chemical reactions. *J. Comput. Phys.*, 22(4):403–434, 1976. doi:10.1016/0021-9991(76)90041-3.

[18] Steven P. Gross, Michael Vershinin, and George T. Shubeita. Cargo transport: Two motors are sometimes better than one. *Current Biology*, 17:R478–R486, 2007.

[19] J. Hattne, D. Fange, and J. Elf. Stochastic reaction-diffusion simulation with MesoRD. *Bioinformatics*, 21:2923–2924, 2005.

[20] Jonathon Howard. The movement of kinesin along microtubules. *Annu. Rev. Physiol.*, 58:703–729, 1996.

[21] Samuel A. Isaacson. The reaction-diffusion master equation as an asymtotic approximation of diffusion to a small target. *SIAM J. Appl. Math.*, 70(1):77–111, 2009.

[22] Kenneth A. Johnson and Susan P. Gilbert. Pathway of the microtubule-kinesin atpase. *Biophys. J.*, 68:173–179, 1995.

[23] N. G. van Kampen. *Stochastic Processes in Physics and Chemistry*. Elsevier, Amsterdam, 5th edition, 2004.

[24] Boris N. Kholodenko. MAP kinase cascade signaling and endocytic trafficking: a marriage of convenience? *Trends Cell Biol.*, 12(4):173–177, 2002.

[25] Boris N. Kholodenko. Four-dimensional organization of protein kinase signaling cascades: the roles of diffusion, endocytosis and molecular motors. *J. Experiment. Biol.*, 2(6):2073–2082, 2003.

[26] Boris N. Kholodenko. Cell-signalling dynamics in time and space. *Nat. Rev. Mol Cell Biol.*, 7(3):165–176, 2006.

[27] Stephen J. King and Trina A. Schroer. Dynactin increases the processivity of the cytoplasmic dynein motor. *Nature Cell Biology*, 2:20–24, 2000.

[28] Sergey Korotov, Michal Křížek, and Pekka Neittaanmäki. Weakened acute type condition for tetrahedral triangulations and the discrete maximum principle. *Math. Comp.*, 70:107–119, 2000.

[29] T. G. Kurtz. Solutions of ordinary differential equations as limits of pure jump Markov processes. *J. Appl. Prob.*, 7:49–58, 1970.

[30] R. J. LeVeque. *Finite Volume Methods for Hyperbolic Problems*. Cambridge University Press, Cambridge, 2002.

[31] Shev F. MacNamara. *Krylov and Finite State Projection Methods for Simulating Stochastic Biochemical Kinetics via the Chemical Master Equation*. PhD thesis, The University of Queensland, Australia, 2008.

[32] M. Malek-Mansour and J. Houard. A new approximation scheme for the study of fluctuations in nonuniform nonequilibrium systems. *Phys. Lett.*, 70A:366–368, 1979.

[33] Roop Mallik and Steven P. Gross. Molecular motors: Strategies to get along. *Current Biology*, 14:971–982, 2004.

[34] Tatiana T. Marquez-Lago and Kevin Burrage. Binomial tau-leap spatial stochastic simulation algorithm for applications in chemical kinetics. *J. Chem. Phys.*, 127(10):104101, 2007.

[35] R. Metzler. The future is noisy: The role of spatial fluctuations in genetic switching. *Phys. Rev. Lett.*, 87:068103, 2001.

[36] Francois Nedelec and Dietrich Foethke. Collective Langevin dymanics of flexible cytoskeletal fibers. *New J. Phys.*, 9:427, 2007.

[37] Jennifer L. Ross, M. Yusuf Ali, and David M. Warshaw. Cargo transport: Molecular motors navigate a complex cytoskeleton. *Curr Opin Cell Biol.*, 20(1):41–47, 2008.

[38] Arne Seitz and Thomas Surrey. Processive movement of single kinesins on crowded microtubules visualized using quantum dots. *The EMBO Journal*, 25(2):267–277, 2006.

[39] Paul Sjöberg, Otto G. Berg, and Johan Elf. Taking the reaction-diffusion master equation to the microscopic limit. *Arxiv preprint arXiv:0905.4629*, 2009.

[40] Ronald D Vale. The molecular motor toolbox for intracellular transport. *Cell*, 112:467–480, 2003.

[41] R. S. Varga. *Matrix Iterative Analysis*. Prentice-Hall, Englewood Cliffs, NJ, 1962.

[42] Michael A. Welte. Bidirectional transport along microtubules. *Current Biology*, 14(525–537), 2004.